 doi:10.20944/preprints202207.0019.v1

Article

Synthesis, Characterization of Magnetic Composites and Testing of Their Activity in Liquid-phase Oxidation of Phenol with Oxygen

Binara Dossumova[1], Tatyana Shakiyeva[1], Dinara Muktaly[1], Larissa Sassykova[1,*], Bedelzhan Baizhomartov[1] and Sendilvelan Subramanian[2]

[1] Al-Farabi Kazakh National University, 71, al-Farabi Ave., Almaty, 050040 Kazakhstan; dosumova63@mail.ru (BD); shakievatatyana@mail.ru (TS); dinara.muktaly@mail.ru (DM); larissa.rav@mail.ru (LR); bedel_b@mail.ru (BB)

[2] Department of Mechanical Engineering, Dr. M.G.R. Educational and Research Institute, University, Chennai, Tamilnadu, 600095 India; sendilvelan.mech@drmgrdu.ac.in

* Correspondence: larissa.rav@mail.ru

Abstract: The development and improvement of methods for the synthesis of environmentally friendly catalysts based on base metals is currently an urgent and promising task of modern catalysis. Catalysts based on nanoscale magnetite and maghemite have fast adsorption-desorption kinetics and high chemical activity. The purpose of this work was to obtain magnetic composites, determine their physicochemical characteristics and verify their activity in the process of liquid-phase oxidation of phenol with oxygen. Magnetic nanocomposites were obtained by chemical co-deposition of salts of ferrous and trivalent iron. The synthesized magnetic composites were studied by X-ray diffractometry, energy dispersive X-ray fluorescence and Mössbauer spectroscopy, IR-Fourier spectroscopy, elemental analysis. To increase the catalytic activity in oxidative processes, the magnetite surfaces were modified using cobalt nitrate salt. Further, $CoFe_2O_4$ was stabilized by adding polyethylenimine (PEI) as a surfactant. Preliminary studies of the oxidation of phenol with oxygen, as the most typical environmental pollutant were carried out on the obtained Fe_3O_4, $CuFe_2O_4$, $CoFe_2O_4$/PEI catalysts. The spectrum of the reaction product shows the presence of CH in the aromatic ring and double C=C bonds, stretching vibrations of the C=O groups of carbonyl compounds; the band at 3059 cm^{-1} corresponds to the presence of double C=C bonds, the band at 3424 cm^{-1} hydroquinone compounds. The band at 1678 cm^{-1} and the intense band at 1646 cm^{-1} refer to vibrations of the C=O bonds of the carbonyl group of benzoquinone. Peaks at 1366 cm^{-1} and 1310 cm^{-1} can be related to the vibrations of C–H and C–C bonds of the quinone ring. Thus it was demonstrated that produced magnetic composites based on iron oxide are quite effective in the oxidation of phenol with oxygen.

Keywords: catalysts; iron oxides; cobalt; oxygen; oxidation; phenol; magnetic composites

1. Introduction

The processes of liquid-phase oxidation of phenols have been comprehensively studied by various scientists [1-15]. As oxidants, depending on which phenol oxidation product should be obtained, it is proposed to use a number of compounds of both organic and inorganic nature. Recently, heterogeneous catalytic oxidation of phenols with air oxygen has become widespread, which has a number of advantages over other methods of destructive oxidation of phenolic compounds. The direction of the oxidation reaction depends on the conditions of the process and the catalyst used. In the processes of destructive oxidation of phenol in the liquid phase, the most popular are: persulfates, peroxides, ozone [1-5, 16-31]. These oxidizers can be introduced into the liquid-phase system from the outside or obtained directly in the reaction volume in situ. It is possible to intensify

Preprints (www.preprints.org) | NOT PEER-REVIEWED | Posted: 1 July 2022 doi:10.20944/preprints202207.0019.v1

the oxidation process by adding various catalytic systems. The use of oxygen as an environmentally friendly and cheap oxidizer for phenol and phenyl-substituted compounds depends on the specificity of the action of catalysts with respect to oxygen. To date, there is a large number of works studying the possibility of deep catalytic oxidation of highly toxic organic compounds, including phenol and phenol-substituted compounds using metallic and metal oxide Pd, Pt, Ru, Rh, Fe, Ni, Si, Co, Mn, as well as deposited catalysts with an active metal content of 0.05-30.0% [10, 20-28].

The development and improvement of methods for the synthesis of environmentally friendly catalysts based on base metal nanoparticles is currently an urgent and promising problem of modern catalysis [32]. Among such catalytic systems, catalysts containing iron nanoparticles and/or iron oxides are of particular interest. This is due to the fact that iron is characterized by low cost, is widely distributed in soils, iron is non-toxic and has unique magnetic properties. Among the oxides of variable metals, iron oxides and their composites are used with great success [33-40]. They are used not only in the field of electronics, medicine, protection and purification of the environment from various pollutants such as phenol and its derivatives, but also due to their cheapness, good thermal stability, high specific surface area as heterogeneous catalysts in complete and partial oxidation reactions. Catalysts based on nanoscale magnetite and maghemite have a high degree of extraction, fast adsorption-desorption kinetics and high chemical activity [33-35, 41-48].

The purpose of this work was to obtain magnetic composites, determine their physico-chemical characteristics and test their activity in the process of liquid-phase oxidation of phenol with oxygen.

2. Materials and Methods

2.1. Preparation of magnetic nanocomposites

Magnetic nanocomposites were obtained by chemical co-deposition of salts of ferrous and trivalent iron. The main advantage of the process of co-deposition of iron salts is that a large number of nanoparticles can be synthesized in this way. The process of co–deposition occurs in two stages: the first is the nucleation of crystals when the concentration reaches a critical supersaturation, and then there is a slow growth of embryos by diffusion of dissolved substances to the crystal surface. To obtain iron oxide nanoparticles, these two stages must be separated, i.e. the nucleation of crystals during the growth period should be avoided [45-52].

Composites were obtained in a Mini glass reactor with a capacity of 50 ml, equipped with a Mini stirrer with a rotation speed controller up to 1500 rpm. An aqueous solution of a mixture of Fe(II) and (III) salts was prepared by stirring at 180 rpm and slowly heated to a temperature of 80°C. Then a 25% ammonia solution was added drop by drop to the prepared solution of iron salts with intensive stirring (600 rpm), controlling the pH of the solution, temperature and stirred for another 30 minutes. The resulting black precipitate of magnetite was washed by decanting with bidistilled water until a pH value of 7-8 was reached, then the magnetic dispersion was centrifuged in a CM-6M centrifuge at 2000 rpm for 10 minutes.

The chemical reaction of the formation of Fe_3O_4 can be written as:

$$Fe^{2+}+2Fe^{3+}+8OH^- = Fe_3O_4+4H_2O \quad (1)$$

In order to increase the catalytic activity in oxidative processes, magnetite surfaces were modified using cobalt nitrate salt, since among spinel ferrites with the general formula is $MeFe_2O_4$, where “Me” is some divalent cation (Fe^{2+}, Co^{2+}, Ni^{2+}, Cu^{2+}) cobalt ferrite ($CoFe_2O_4$) has a stronger cubic magnetocrystalline anisotropy.

To obtain $CoFe_2O_4$, a mixture of aqueous solutions of $FeCl_3{\cdot}6H_2O$ and $Co(NO_3)_2{\cdot}6H_2O$ at 180 rpm was slowly heated to a temperature of 80°C. Then a 25% ammonia solution was added drop by drop to the prepared solution with intensive stirring (600 rpm), controlling the pH of the solution, the temperature and stirred another 40 min.

Preprints (www.preprints.org) | NOT PEER-REVIEWED | Posted: 1 July 2022 doi:10.20944/preprints202207.0019.v1

At the same time, an instantaneous formation of a dark brown suspension was observed. The reaction was carried out at a temperature of 80° ± 5°C, the temperature was kept constant in the process with the need to obtain nanodisperse ferrite composites. The resulting precipitates were washed by decantation in a rotary evaporator and dried at a temperature of 90-100°C.

The chemical reaction of $CoFe_2O_4$ formation can be written as:

$$Co^{2+} + 2Fe^{3+} + 8OH^- = CoFe_2O_4 + 4H_2O \quad (2)$$

Further, $CoFe_2O_4$ was stabilized by adding polyethylenimine as a surfactant, hybrid materials based on cobalt ferrite and polyethylenimine (PEI) were obtained by mixing an aqueous suspension of cobalt ferrite and an aqueous solution of PEI at the same temperature at which cobalt ferrite synthesis was carried out, and mixed at the specified temperature for 1.5 hours. The resulting composites were then dried at room temperature in air. As a result, samples of hybrid materials $CoFe_2O_4$, $CoFe_2O$/PEI were obtained.

2.2. Tests of synthesized catalysts in the process of oxidation of phenol with oxygen

Preliminary studies of the oxidation of phenol with oxygen, as the most typical environmental pollutant, were carried out on the obtained Fe_3O_4, $CoFe_2O_4$, $CoFe_2O_4$/PEI catalysts.

The oxidation reactions of phenol with oxygen were carried out in a non-flowing glass gradient-free thermostatic reactor of "the duck" type (Figure 1) equipped with a potentiometric device. The kinetic regime was provided by intensive shaking of the reactor (300-400 swings per minute), the volume of the liquid phase was no more than 40 cm^3, with a total reactor volume of 180 cm^3. The reaction rate was monitored by oxygen absorption from a thermostatic burette connected to the reactor.

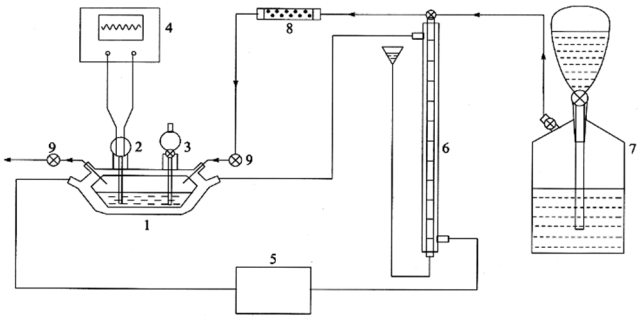

Figure 1. Laboratory installation for oxidation of phenol with oxygen: 1- reactor, 2- electrode, 3-funnel for reagent input, 4-potentiometer, 5-thermostat, 6- measuring burette, 7- gasometer, 8-transition valve, 9- taps.

The components of the system were introduced in the following order: solutions of substances were poured into the reactor, the interactions between which are limited by equilibrium processes in the liquid phase, or the speed of which can be neglected compared to the speed of the reaction under study. Then a given oxygen atmosphere was created in the reactor. The reactor was shaken until a constant volume of the gas phase was established, within the experimental error, after which the remaining components of the system were quickly introduced through a glass faucet. This moment was taken as the beginning of the reaction. The temperature was maintained with an accuracy of 0.5°C using a thermostat.

When the oxygen absorption rate became below 0.1 ml/min, the reaction was considered complete. Samples were taken at certain intervals, which were analyzed for the content of phenol and benzoquinone by UV and IR spectroscopy.

Preprints (www.preprints.org) | NOT PEER-REVIEWED | Posted: 1 July 2022 doi:10.20944/preprints202207.0019.v1

The reactions were carried out under optimal conditions established during the studies of phenol transformation in the presence of the obtained catalysts. The initial concentration of phenol was 0.003 mol/l.

2.3. Conducting an analysis

The obtained magnetic composites were studied by X-ray diffractometry, energy dispersive X-ray fluorescence spectroscopy, and Mössbauer, IR-Fourier spectroscopy. Mössbauer spectroscopy was used to study the magnetic structure and phase analysis. The source was ^{57}Co in a rhodium matrix with an activity of 100 mCi. The spectra were processed on a PC using "the least squares" method. The values of isomeric shifts (Is) are given relative to α-Fe. The temperature of taking spectra is 20°C. Shooting mode is "in transmission". Spectrometer MS 1104Em was applied. $\Delta IS = \pm 0.03$ mm/s; $\Delta QS = \pm 0.03$ mm/s; $\Delta S = \pm 2.0$ %.

Elemental analysis was performed using energy-dispersive X-ray fluorescence spectroscopy on an INCA Energy 450 energy-dispersive microanalysis system mounted on a JSM 6610 LV scanning electron microscope, JOEL, Japan. Determination error is ± 0.01%.

X-ray diffractometry was performed using a Dron-4-07 X-ray diffractometer with a tube with a cobalt anode. Shooting mode: sweep speed 2 degrees/min; operating parameters of the tube: 30 kV, 20 mA.

IR spectra were recorded and processed on a VERTEX 70 IR-Fourier spectrometer in the frequency range from 4000 to 500 cm^{-1} and using a PIKE MIRacle ATR single frustrated internal total reflection (ATR) attachment with a germanium crystal. The results were processed using the OPUS 7.2.139.1294 software.

The absorption spectra were measured using a Shimadzu UV-1240 spectrophotometer with a spectrum measurement range from 190 to 1100 nm.

3. Results

3.1. Characterization of magnetic composites

Figure 2 shows an X-ray diffractogram of a magnetic composite. The X-ray image of synthesized iron oxide nanoparticles agrees well with the literature data for magnetite [44-46, 52-55]. Reflexes at 2θ values 35°, 43°, 57°, 63° and 74° corresponds to the lattice planes (311), (400), (422), (511), and (440), respectively, characteristic of iron oxide, indicating its crystal structure. However, the positions of the diffraction peaks of magnetite and maghemite are very much the same and they have a common crystal lattice structure.

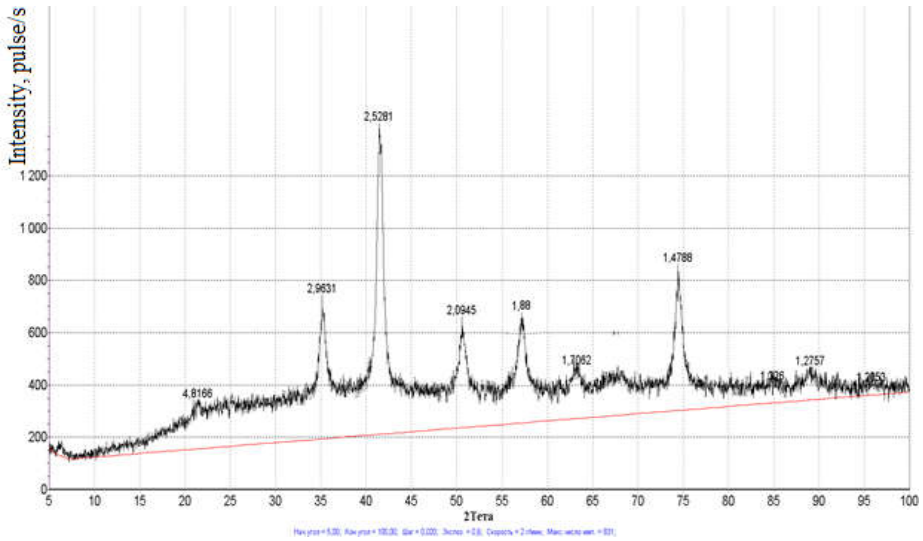

Figure 2. X-ray diffractogram of synthesized iron oxide, magnetic composite.

Preprints (www.preprints.org) | NOT PEER-REVIEWED | Posted: 1 July 2022 doi:10.20944/preprints202207.0019.v1

The structure of maghemite is a defective structure of magnetite, a cation-deficient form of spinel. Mössbauer spectroscopy allows us to solve the problem of phase analysis in magnetic composites, therefore, using Mössbauer spectroscopy, we have studied the structure and phase composition of magnetic composites.

Figure 3 shows the Mössbauer spectrum of a composite obtained at room temperature belonging to iron oxides in a magnetically ordered state.

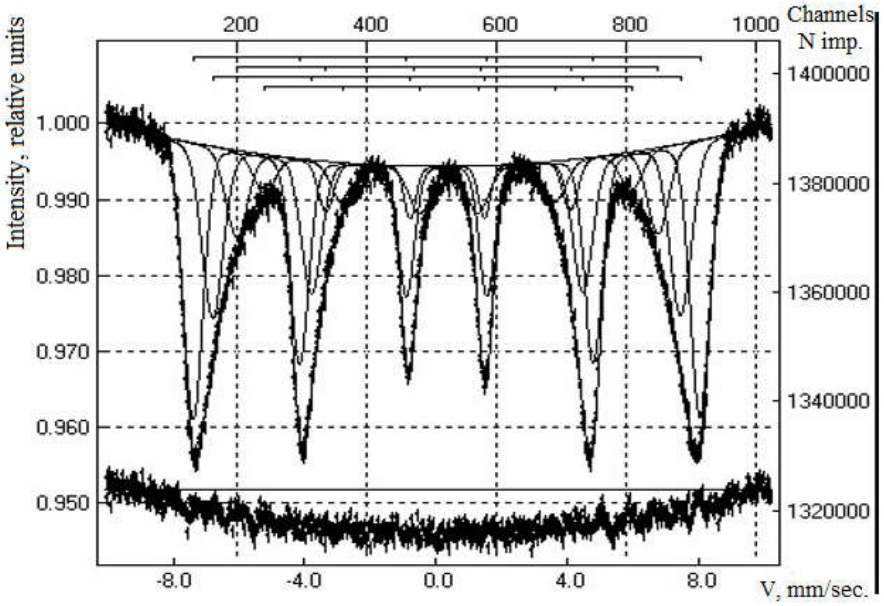

Figure 3. Mössbauer spectrum of a magnetic composite at 20°C.

The Mössbauer spectrum has a relaxation character, as indicated by the parabolic shape of the background line. The magnetic hyperfine splitting of resonance lines indicates the magnetically ordered states of iron ions at room temperature. Satisfactory fit of the calculated spectrum to the experimental one was obtained by decomposing the latter into four magnetically ordered components (phases) with a distribution of effective magnetic fields (Heffective) from 485 to 397 keV.

The spectrum can be considered as two sextets similar in their parameters, corresponding to trivalent iron ions and with slightly less splitting from divalent iron ions. The values of isomeric shifts (Is) and quadrupole cleavages (Qs) indicate the simultaneous presence of phases of magnetite Fe_3O_4 and maghemite γ-Fe_2O_3, which completely coincide with the tabular values. The values of the isomeric shift and the effective ultrathin magnetic field obtained from the experimental Mössbauer spectra correspond to ^{57}Fe nuclei occupying tetrahedral and octahedral positions. The low values of the effective magnetic fields can be explained by the high dispersion of the sample particles. This possibility is indicated by the relaxation nature of the spectrum. In this case, the size of the studied particles is close to 10 nm [52-58].

To determine the chemical composition of magnetic composites, an elemental analysis was carried out. Figure 4 and Figure 5 show the results of SEM (Scanning Electron Microscopy) with the corresponding spectra of energy dispersion analysis.

Preprints (www.preprints.org) | NOT PEER-REVIEWED | Posted: 1 July 2022 doi:10.20944/preprints202207.0019.v1

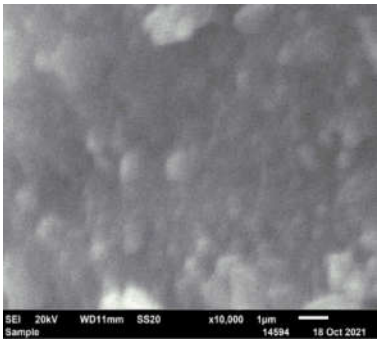

Figure 4. SEM image of magnetic composite.

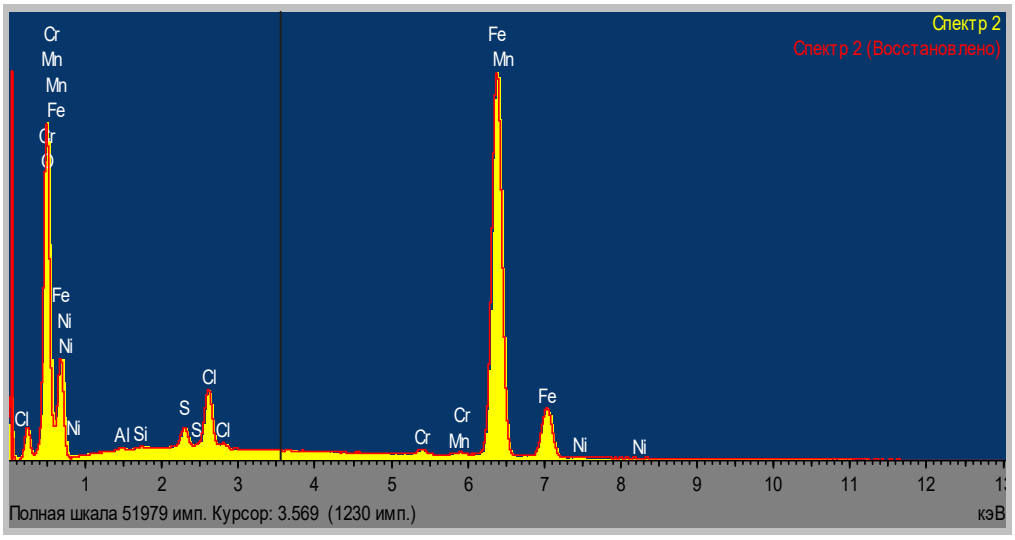

Figure 5. X-ray fluorescence spectrum of magnetic composite.

The elemental analysis of magnetic composite is shown in Table 1. Processing parameters: all elements were analyzed (normalized).

Table 1. Data of elemental analysis of magnetic composite (in wt.%).

Area	Elements								
	O	Al	Si	S	Cl	Cr	Mn	Fe	Total
Area 1	26.51	0.15	0.13	1.13	1.27	0.47	0.40	69.94	100.00
Area 2	26.52	0.12	0.13	0.87	1.34	0.50	0.30	70.22	100.00
Area 3	26.21	0.15	0.11	1.00	1.33	0.47	0.33	70.38	100.00
Average	26.42	0.14	0.12	1.00	1.31	0.48	0.34	70.18	100.00

The IR spectrum of the composite contains wide bands of valence vibrations with absorption maxima of 3380 cm^{-1} and deformation vibrations of 1637 cm^{-1}, indicating the presence of hydroxyl groups. In the IR spectrum of the magnetic composite, an absorption band is observed at 1111 cm^{-1} and a shoulder at 1051 cm^{-1}, according to the literature data, which can be identified as deformation vibrations of Fe–O–H bonds in the spinel structure. Valence fluctuations of the Fe – O bond in oxides are manifested in the region of 800-600 cm^{-1} at 783.649 cm^{-1}.

Figure 6 and Figure 7 show the X-ray diffraction patterns of $CoFe_2O_4$ and $CoFe_2O_4$/PEI composites, respectively. In the diffraction pattern of $CoFe_2O_4$ (Figure 6), along with reflections related to iron oxide, a cobalt reflex appears in the region of angles 2θ = 50-55° and an indistinguishable shoulder in the region 2θ = 40-45°. When stabilized with polyethyleneimine, the reflex diffraction patterns revealed several phases of iron

Preprints (www.preprints.org) | NOT PEER-REVIEWED | Posted: 1 July 2022 doi:10.20944/preprints202207.0019.v1

oxides - γ-Fe_2O_3, α-Fe_2O_3, ε-Fe_2O_3. The diffraction reflections for cobalt oxide correspond to spinel Co_3O_4 [37, 38, 42, 57-60].

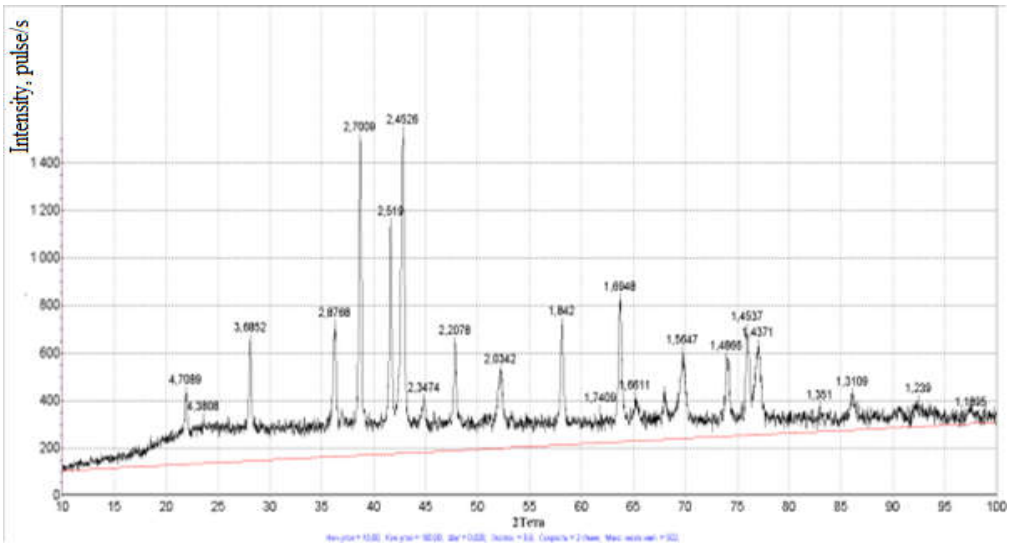

Figure 6. X-ray diffraction pattern of $CoFe_2O_4$ composite.

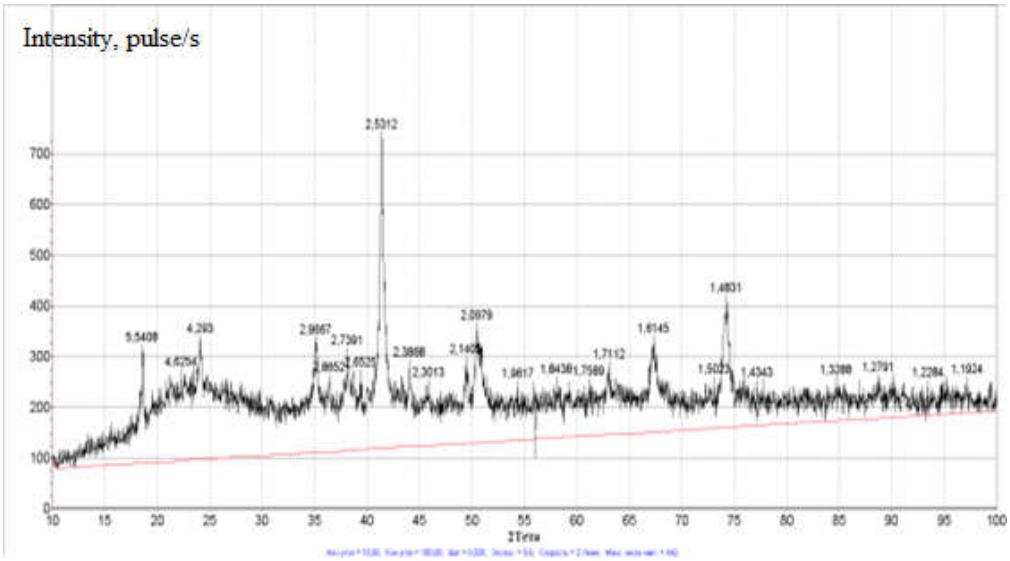

Figure 7. X-ray diffraction pattern of $CoFe_2O_4$/PEI composite.

Figure 8 and Figure 9, Table 2 show the Mössbauer spectrum of composites obtained at room temperature belonging to iron oxides in a magnetically ordered state.

The substitution of the Fe atom for the Co atom leads to an increase in the hyperfine magnetic field at the ^{57}Fe nucleus. The Mössbauer spectroscopy data confirm the results of X-ray phase analysis. We assume that during the process, the decrease in the values of H effective (keV) in $CoFe_2O_4$/PEI compared to $CoFe_2O_4$ is associated with a high dispersion of sample particles during the addition of PEI. The values of the shifts observed in the spectra make it possible to identify them as partial spectra of the Fe^{2+} and Fe^{3+} cations in the paramagnetic state.

Preprints (www.preprints.org) | NOT PEER-REVIEWED | Posted: 1 July 2022 doi:10.20944/preprints202207.0019.v1

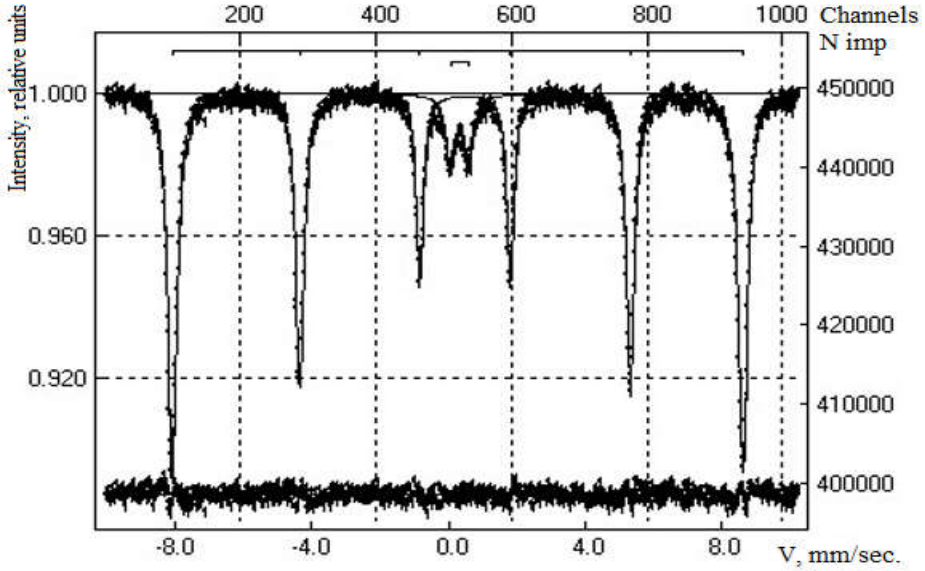

Figure 8. Mössbauer spectrum of $CoFe_2O_4$.

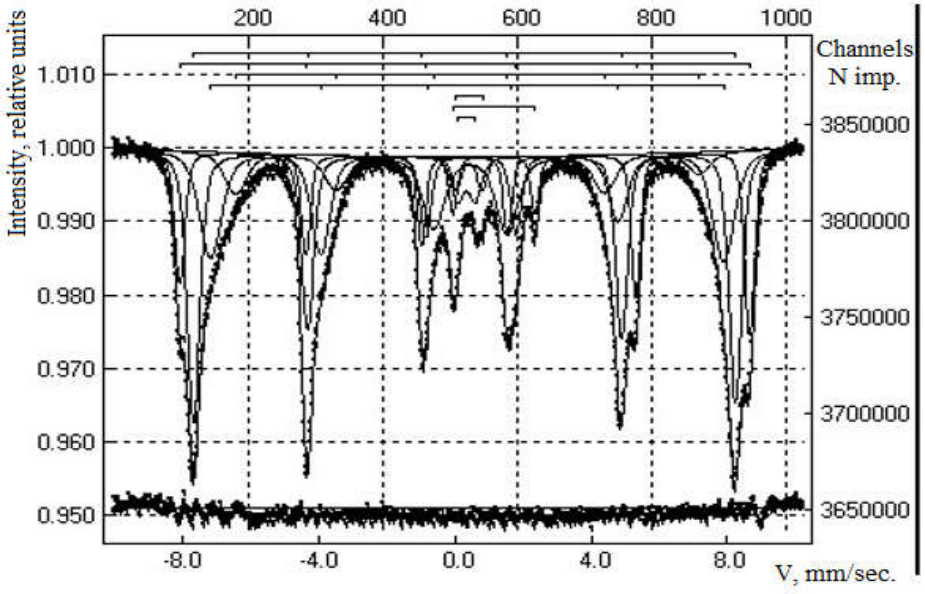

Figure 9. Mössbauer spectrum of $CoFe_2O_4$/PEI.

Table 2. Results of Mössbauer spectra of $CoFe_2O_4$, $CoFe_2O_4$/PEI composites.

Sample	IS, (mm·s^{-1})	QS (mm·s^{-1})	$H_{effective}$ (keV)	S (%)
Composite $CoFe_2O_4$	0.37	- 0.22	518	92
	0.31	0.54	-	8.0
Composite $CoFe_2O_4$/PEI	0.37	-0.18	520	20.0
	0.28	-0.01	495	34.0
	0.41	-0.09	423	17.0
	0.39	-0.07	469	21.0
	0.42	0.76	-	2.0
	1.15	2.42	-	3.0
	0.34	0.53	-	3.0

The chemical composition of $CoFe_2O_4$ was also determined.

Preprints (www.preprints.org) | NOT PEER-REVIEWED | Posted: 1 July 2022 doi:10.20944/preprints202207.0019.v1

Figure 10 and Figure 11 show the results of scanning electron microscopy with the corresponding energy dispersive analysis spectra.

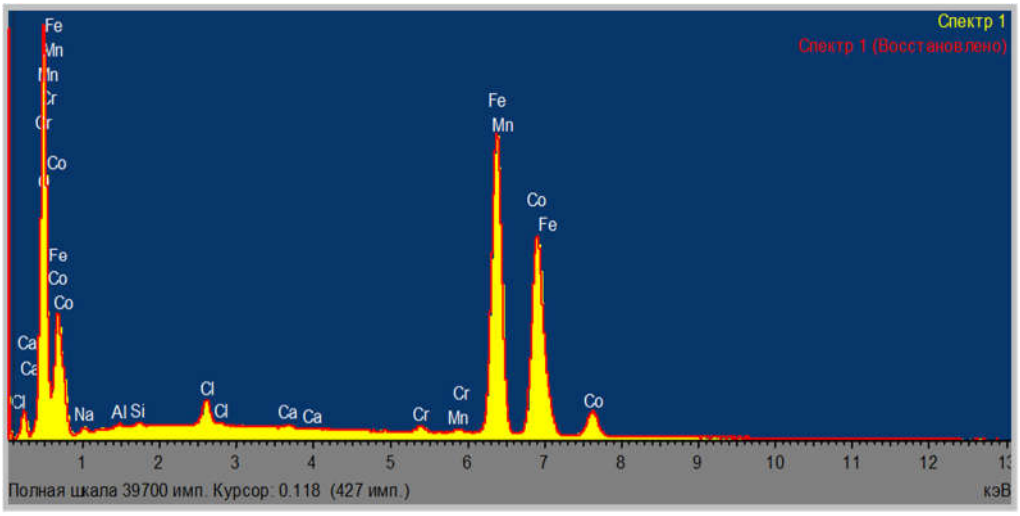

Figure 10. X-ray fluorescence spectrum of $CoFe_2O_4$.

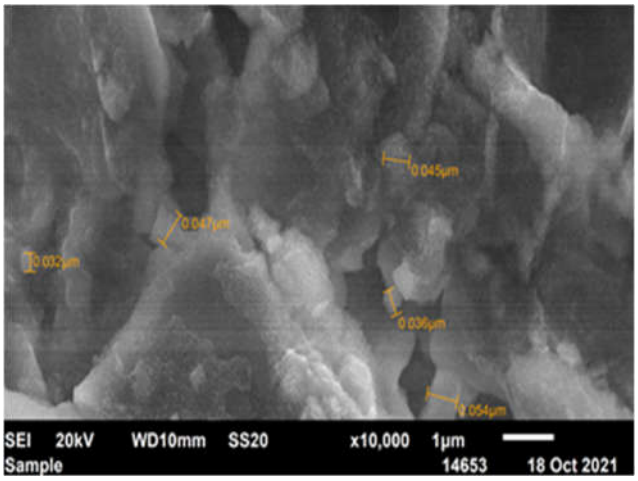

Figure 11. SEM image of $CoFe_2O_4$.

Elemental analysis is presented in Table 3. Processing parameters: all elements were analyzed (normalized).

Table 3. Data of elemental analysis of $CoFe_2O_4$ (in wt.%).

Area	Elements									
	O	Al	Si	Cl	Ca	Cr	Mn	Fe	Co	Total
Area 1	21.16	0.17	0.12	14.68	0.03	0.19	0.22	43.28	20.15	100.00
Area 2	21.29	0.14	0.11	13.76	0.05	0.22	0.14	42.48	21.80	100.00
Area 3	20.69	0.15	0.13	14.81	0.18	0.27	0.24	42.56	20.98	100.00
Average	21.05	0.15	0.12	14.42	0.09	0.23	0.20	42.77	20.98	100.00

The IR spectrum of $CoFe_2O_4$ contains wide bands of valence oscillations with absorption maxima of 3388 cm^{-1} and deformation oscillations of 1607 cm^{-1}, indicating the presence of hydroxyl groups. The absorption band is observed at 1031 cm^{-1} and 678-663 cm^{-1}, according to the literature data, which can be identified as valence oscillations of the Co-O-H and Co–O bonds, respectively. Deformation fluctuations of Fe-O-H bonds in the spinel structure are manifested at 1355, 1219 cm^{-1}. Valence vibrations of the Fe-O bond in oxides

Preprints (www.preprints.org) | NOT PEER-REVIEWED | Posted: 1 July 2022 doi:10.20944/preprints202207.0019.v1

manifest themselves in the region of 800-600 cm^{-1} in the form of several bands at 735, 656, 639, 626 cm^{-1}.

When identifying the IR spectra of $CoFe_2O_4$/PEI, in addition to the absorption bands Co-O and Fe-O, Fe-O-H absorption bands in the region of 1105 and 1048 cm^{-1} corresponding to the valence oscillations of C–N and CH_2, respectively, are observed. The shift of the absorption bands with respect to the PEI spectrum is observed, as well as the shift of the bands characteristic of the bonds of the NH group in the region of 1649 cm^{-1}. The complexity of the spectra in this area did not allow us to find out the participation of PEI in the formation of complexes with metal ions [51-62].

3.2. Results of testing the synthesized catalysts in the oxidation of phenol with oxygen

The obtained Fe_3O_4, $CoFe_2O_4$, $CoFe_2O_4$/PEI were investigated as catalysts in the oxidation of phenol as the most typical environmental pollutant.

The initial concentration of phenol was 0.003 mol/L.

Figure 12 shows that the most effective oxidation of phenol occurs at $CoFe_2O_4$/PEI.

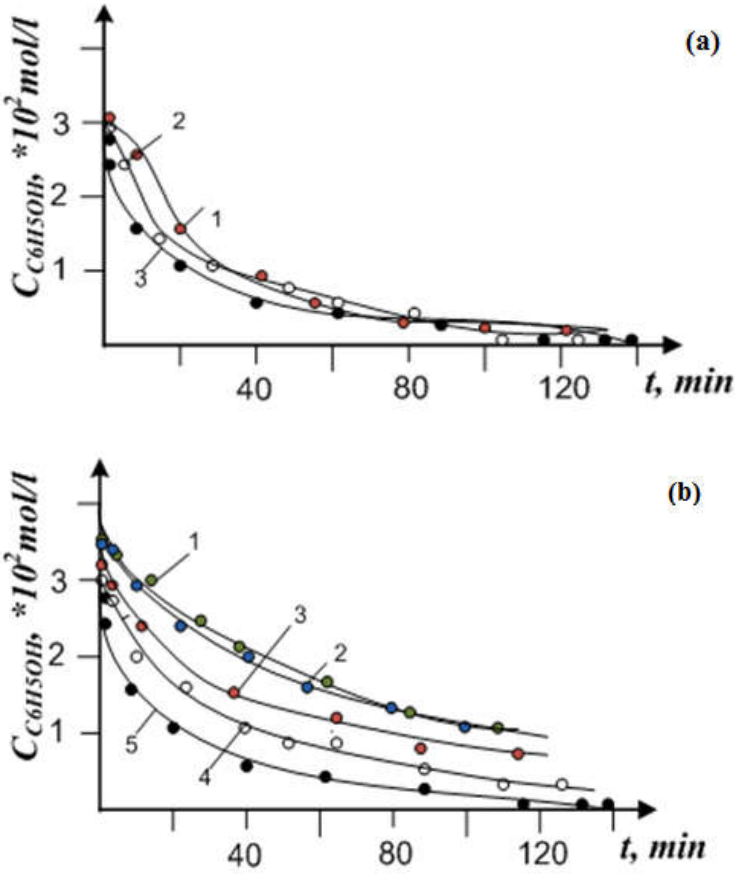

Figure 12. Dependence of phenol concentration on oxidation time: a) in the presence of 1-Fe_3O_4, 2-$CoFe_2O_4$, 3-$CoFe_2O_4$/PEI; b) in the presence of $CoFe_2O_4$/PEI: 1 – 30°C; 2 - 40°C; 3 - 50°C; 4 - 60°C; 5 - 80°C.

When phenol is oxidized to $CoFe_2O_4$ stabilized with polyethylenimine, the concentration of phenol decreases from 0.03 to 0.001 mol/L in 120 minutes, on Fe_3O_4, $CoFe_2O_4$ catalytic systems, phenol oxidation occurs with a decrease in the concentration of phenol from 0.03 to 0.0025 mol/L in 150 minutes. With an increase in temperature from 30°C to 80 °C, the maximum degree of transformation of C_6H_5H is observed at 80°C.

In the UV spectrum of the initial solution of phenol, absorption bands are observed in the region of 193, and 210.8 and 270 nm (Fig. 13, a) characteristic of phenol. Depending on the oxidation time in the UV spectra, a shoulder in the region of 207 nm (Fig. 13b) and

Preprints (www.preprints.org) | NOT PEER-REVIEWED | Posted: 1 July 2022 doi:10.20944/preprints202207.0019.v1

a plateau in the region of 275 nm are similarly observed. The ratio of intensities and spectral characteristics of the absorption bands of phenol with a shift to the long-wavelength region from absorption measurements in the wavelength range 190-320 nm allows us to estimate the concentration of phenol in the sample, to give a primary qualitative assessment of the oxidation of phenol.

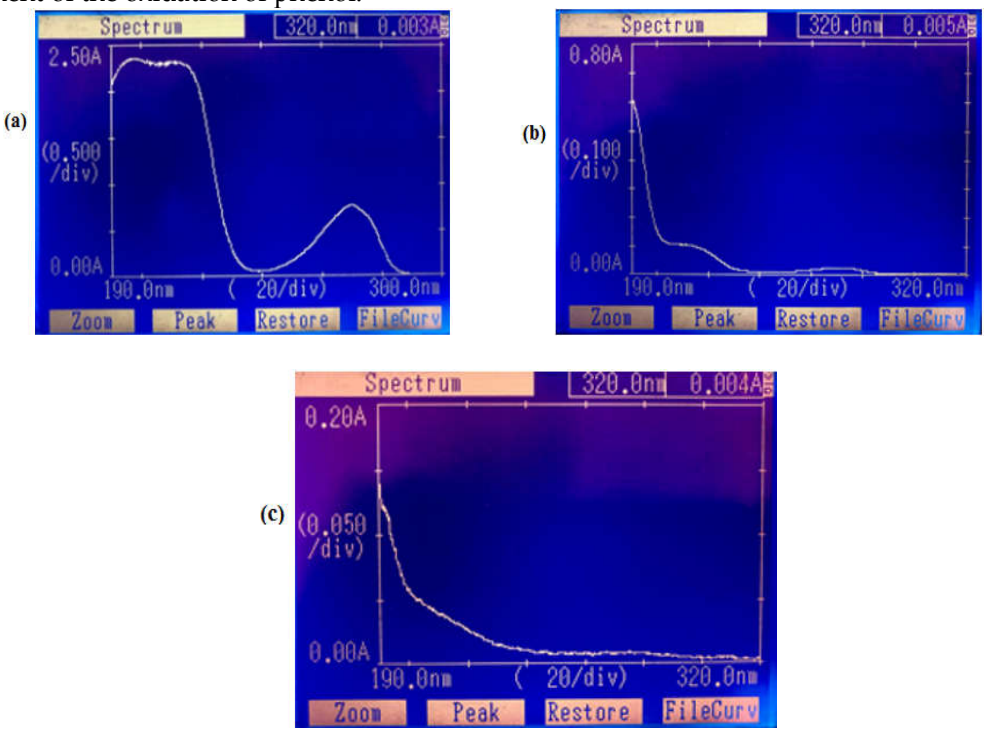

Figure 13. Absorption spectra of the initial aqueous solution of phenol (a) and oxidation time (b, 1 hour); (c, 2.0 hours).

The IR spectra of phenol and reaction products are shown in Figure 14. In the IR spectra of phenols, the characteristic absorption bands of valence vibrations of the OH group lie in the frequency range 3390-3600 cm^{-1}, valence vibrations of the C-O group are observed at 1230 cm^{-1}. In the UV spectra, the absorption bands of phenol are as follows: 210 (ε = 6200 L/mol · cm) and 270 nm (ε = 1450 L/mol · cm).

Preprints (www.preprints.org) | NOT PEER-REVIEWED | Posted: 1 July 2022 doi:10.20944/preprints202207.0019.v1

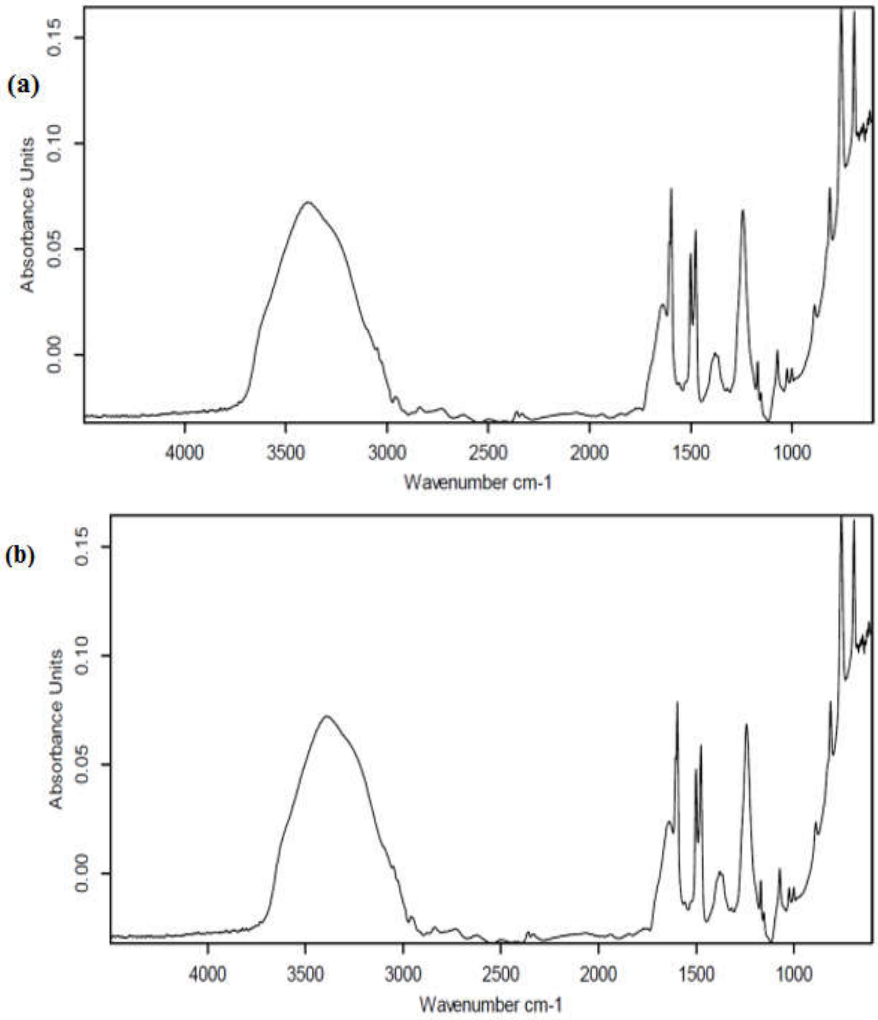

Figure 14. IR spectra of the initial aqueous solution of phenol before (a) and after (b) reactions.

In the IR spectrum of the phenol solution, characteristic absorption bands of the OH group valence oscillations in the region of 3394 cm^{-1} are observed and the band in the region of 1242 cm^{-1} refers to the valence vibrations of the C–O groups of phenol (Fig.14a).

A qualitative comparison of the obtained spectra of the reaction product shows the presence of CH in the aromatic ring and double C =C bonds, valence vibrations of C= O groups of carbonyl compounds, the band 3059 cm^{-1} corresponds to the presence of double C=C bonds, the band 3424 cm^{-1} may refer to vibrations of hydroxyl groups of the intermediate compound hydroquinone. The band in the region of 1678 cm^{-1} and the intense band in the region of 1646 cm^{-1} refers to fluctuations in the bonds of the C=O carbonyl group of benzoquinone [40-44, 59-62]. The peaks of 1366 cm^{-1} and 1310 cm^{-1} may relate to fluctuations in the C-H and C-C bonds of the quinone ring (Fig.14b).

Thus, according to the data of UV and IR spectroscopy, magnetic composites based on iron oxide show their good effectiveness in the oxidation of phenol with oxygen.

The research will be continued.

4. Conclusions

The work is aimed at creating magnetic nanocomposites for the oxidation of the organic pollutant phenol and its derivatives. Magnetic nanocomposites were obtained by chemical co-precipitation of ferrous and trivalent iron salts. The co-precipitation process consisted of two stages: the nucleation of crystals, when the concentration reaches a critical supersaturation, and the slow growth of nuclei by diffusion of solutes to the crystal

surface. Magnetite surfaces were modified with cobalt nitrate salt. Next, polyethyleneimine (PEI) was added to $CoFe_2O_4$ as a surfactant. The composition and structure of the catalysts have been characterized using modern physicochemical methods. The study of the characteristics of magnetically active nanocomposites was carried out using electron microscopy, Mössbauer, IR-Fourier spectroscopy. The developed nanomagnetic composites were tested in the process of phenol oxidation in aqueous solutions. UV and IR spectroscopy data confirm that magnetic composites based on iron oxide are active and efficient in the oxidation of phenol with oxygen.

Author Contributions: Conceptualization, D. M. and T. S.; methodology, B. D. and T. S.; software, B. B. and L. S.; validation, T.S., L.S. and S.S.; formal analysis, D.M. and L.S.; investigation, B.D., B. B. and T. S.; resources, T.S. and B.D.; data curation, T.S. and B. D.; writing—original draft preparation, B. D., T. S., S. S. and L.S.; writing—review and editing, L.S., S.S. and B.D.; visualization, L.S. and B.B.; supervision, B.D., T.S., D.M. and L.S.; project administration, T. S.; funding acquisition, B. D., T. S. and D.M. All authors have read and agreed to the published version of the manuscript.

Funding: "This research was funded by grant funding under the program: "No. AP09260687 Technology for the recovery and disposal of toxic compounds from industrial wastewater".

Conflicts of Interest: The authors declare no conflict of interest.

References

1. Maurya, M.R.; Titinchi, S.J.J.; Chand, S. Oxidation of phenol with H2O2 catalysed by Cr(III), Fe(III) or Bi(III) N,N'-bis(salicylidene)diethylenetriamine (H2saldien) complexes encapsulated in zeolite-Y. *J. Mol. Catal. A Chem* **2003**. *193(1-2)*, 165-176.
2. Barrault, J. Catalytic wet peroxide oxidation over mixed (Al–Fe) pillared clays. *Appl. Catal. B* **2000**. *27(4)*, L225-L230. https://doi.org/10.1016/s0926-3373(00)00170-3.
3. Guélou, E.; Barrault, J.; Fournier, J.; Tatibouët, J.M. Active iron species in the catalytic wet peroxide oxidation of phenol over pillared clays containing iron. *Appl. Catal. B* **2003**. *44(1)*, 1-8. https://doi.org/10.1016/s0926-3373(03)00003-1.
4. Carriazo, J.; Guélou, E.; Barrault, J.; Tatibouët, J.M.; Molina, R.; Moreno, S. Catalytic wet peroxide oxidation of phenol by pillared clays containing Al–Ce–Fe. *Water Res.* **2005**. *39(16)*, 3891-3899. https://doi.org/10.1016/j.watres.2005.06.034.
5. Zazo, J. A.; Casas, J. A.; Mohedano, A. F.; Gilarranz, M. A.; Rodríguez, J. J. Chemical Pathway and Kinetics of Phenol Oxidation by Fenton's Reagent. *Environ. Sci. Technol*. **2005**. *39(23)*, 9295-9302. https://doi.org/10.1021/es050452h.
6. Guo, J.; Al-Dahhan, M. Catalytic wet air oxidation of phenol in concurrent downflow and upflow packed-bed reactors over pillared clay catalyst. *Chem. Eng. Sci.* **2005**, *60(3)*, 735-746. https://doi.org/10.1016/j.ces.2004.08.043.
7. Krajnc, M.; Levec, J. Oxidation of Phenol over a Transition-Metal Oxide Catalyst in Supercritical Water. Ind. Eng. Chem. Res. 1997, 36(9), 3439-3445. https://doi.org/10.1021/ie9701130.
8. Tashmukhambetova, Zh Kh; Sassykova, LR; Aubakirov, YA; Dangaliyeva, A Kh; Kanatbayeva, MA; Rustem, AE. New catalysts for toluene oxidation technology in the liquid phase. *Mater Today: Proc.* **2020**, *31(3)*, 529-531. https://doi.org/10.1016/j.matpr.2020.06.141.
9. Cosgrove, W. J.; Loucks, D. P. Water management: current and future challenges and research directions. *Water Resour. Res.* **2015**, *51(6)*, 4823–4839.
10. Guo, J.; Al-Dahhan, M. Kinetics of Wet Air Oxidation of Phenol over a Novel Catalyst. *Ind. Eng. Chem. Res*. **2003**, *42(22)*, 5473-5481. https://doi.org/10.1021/ie0302488.
11. Arefieva, O. D.; Vasilyeva, M. S.; Kuryavy, V. G.; Ustinov, A. Yu.; Zemnukhova, L. A.; Gushchina, D. D. Oxidative destruction of phenol on Fe/SiO_2 catalysts. *Water Sci Technol Water Supply* **2020**, *81(10)*, 2189- 2201. https://doi.org/10.2166/wst.2020.277.
12. Guo, J.; Al-Dahhan, M. Catalytic Wet Oxidation of Phenol by Hydrogen Peroxide over Pillared Clay Catalyst. *Ind. Eng. Chem. Res.* **2003**, *42(12)*, 2450-2460. https://doi.org/10.1021/ie020344t.
13. Tomita, K.; Oshima, Y. Stability of Manganese Oxide in Catalytic Supercritical Water Oxidation of Phenol, *Ind. Eng. Chem. Res.* **2004**, *43(24)*, 7740-7743. https://doi.org/10.1021/ie040154d.
14. M. Álvarez, P.; McLurgh, D.; Plucinski, P. Copper Oxide Mounted on Activated Carbon as Catalyst for Wet Air Oxidation of Aqueous Phenol. 2. Catalyst Stability. *Ind. Eng. Chem. Res.* **2002**, *41(9)*, 2153-2158. https://doi.org/10.1021/ie010447w.
15. Atoguchi, T.; Yao, S. Phenol oxidation over titanosilicalite-1: experimental and DFT study of solvent. *J Mol Catal A Chem.* **2001**, *176(1-2)*, 173-178. https://doi.org/10.1016/s1381-1169(01)00255-2.
16. Guerra, R. Ecotoxicological and chemical evaluation of phenolic compounds in industrial effluents. *Chemosphere* **2001**, *44(8)*, 1737-1747. https://doi.org/10.1016/s0045-6535(00)00562-2.
17. Quintanilla, A.; Casas, J.; Mohedano, A.; Rodriguez, J. Reaction pathway of the catalytic wet air oxidation of phenol with a Fe/activated carbon catalyst. *Appl. Catal. B* **2006**. *67(3-4)*, 206-216. https://doi.org/10.1016/j.apcatb.2006.05.003.
18. Rey, A.; Faraldos, M.; Casas, J.A.; Zazo, J.A.; Bahamonde, A.; Rodríguez, J.J. Catalytic wet peroxide oxidation of phenol over Fe/AC catalysts: Influence of iron precursor and activated carbon surface. *Appl. Catal. B* **2009**, *86(1-2)*, 69-77. https://doi.org/10.1016/j.apcatb.2008.07.023.

19. Wu, Q.; Hu, X.; Yue, P. Kinetics study on catalytic wet air oxidation of phenol. *Chem. Eng. Sci.* **2003**, *58(3-6)*, 923-928. https://doi.org/10.1016/s0009-2509(02)00628-0.
20. Santos, A.; Yustos, P.; Quintanilla, A.; García-Ochoa, F. Influence of pH on the wet oxidation of phenol with copper catalyst. *Top Catal.* **2005**, *33(1-4)*, 181-192. https://doi.org/10.1007/s11244-005-2524-2.
21. Santos, A.; Yustos, P.; Quintanilla, A.; Garcia-Ochoa, F. Kinetic model of wet oxidation of phenol at basic pH using a copper catalyst. *Chem. Eng. Sci.* **2005**, *60(17)*, P.4866-4878. https://doi.org/10.1016/j.ces.2005.04.015.
22. Santos, A.; Yustos, P.; Cordero, T.; Gomis, S.; Rodríguez, S.; García-Ochoa, F. Catalytic wet oxidation of phenol on active carbon: stability, phenol conversion and mineralization. *Catal. Today* **2005**, *102-103*, 213-218. https://doi.org/10.1016/j.cattod.2005.02.006.
23. Cordero T., Rodríguez-Mirasol J., Bedia J., Gomis S., Yustos P., García-Ochoa F., Santos, A. Activated carbon as catalyst in wet oxidation of phenol: Effect of the oxidation reaction on the catalyst properties and stability. *Appl. Catal. B* **2008**, *81(1-2)*, 122-131. https://doi.org/10.1016/j.apcatb.2007.12.010.
24. Santos, A.; Yustos, P.; Quintanilla, A.; Rodríguez, S.; García-Ochoa, F. Route of the catalytic oxidation of phenol in aqueous phase. *Appl. Catal. B* **2002**, *39(2)*, 97-113. https://doi.org/10.1016/s0926-3373(02)00087-5.
25. Dosumov, K.; Ergazieva, G.E. Morphology and activity of vanadium-containing catalysts for the selective oxidation of benzene to maleic anhydride, *Russ. J. Phys. Chem.A* **2012**. *86*, 1766–1768. https://doi.org/10.1134/S0036024412110106.
26. Santos, A.; Yustos, P.; Durbán, B.; García-Ochoa, F. Oxidation of phenol in aqueous solution with copper catalysts. *Catal. Today* **2001**, *66(2-4)*, 511-517. https://doi.org/10.1016/s0920-5861(00)00623-4.
27. Stüber, F.; Polaert, I.; Delmas, H.; Font, J.; Fortuny, A.; Fabregat, A. Catalytic wet air oxidation of phenol using active carbon: performance of discontinuous and continuous reactors. *J. Chem. Technol. Biotechnol.* **2001**, *76(7)*, 743-751. https://doi.org/10.1002/jctb.441.
28. Cao, S.; Chen, G.; Hu, X.; Yue, P. L. Catalytic wet air oxidation of wastewater containing ammonia and phenol over activated carbon supported Pt catalysts. *Catal. Today* **2003**, *88(1-2)*, 37-47. https://doi.org/10.1016/j.cattod.2003.08.005.
29. Rey, A.; Hungria, A.B.; Duran-Valle, C.J.; Faraldos, M.; Bahamonde, A. ; Casas, J.A.; Rodriguez, J.J. On the optimization of activated carbon-supported iron catalysts in catalytic wet peroxide oxidation process. *Appl. Catal. B* **2016**, *181*, 249-259. https://doi.org/10.1016/j.apcatb.2015.07.051
30. Garcia-Costa, A.L.; Zazo, J.A.; Rodriguez, J.J.; Casas, J. A. Microwave-assisted catalytic wet peroxide oxidation. Comparison of Fe catalysts supported on activated carbon and γ-alumina. *Appl. Catal. B* **2017**, 218(5), 637-642. https://doi.org/10.1016/j.apcatb.2017.06.058.
31. Zazo J.A., Casas J.A., Mohedano A.F., Rodríguez J.J. Catalytic wet peroxide oxidation of phenol with a Fe/active carbon catalyst. *Appl. Catal. B* **2006**, 65(3-4), 261-268. https://doi.org/10.1016/j.apcatb.2006.02.008.
32. Polshettiwar, V.; Varma, R. S. Green chemistry by nano-catalysis, *Green Chem.* **2010**, *12(5)*, 743. https://doi.org/10.1039/b921171c
33. Laurent, S.; Forge, D.; Port, M.; Roch, A.; Robic, C.; Elst, L.V.; Muller, R.N. Magnetic Iron Oxide Nanoparticles: Synthesis, Stabilization, Vectorization, Physicochemical Characterizations, and Biological Applications. *Chem. Rev.* **2008**, *108(6)*, 2064-2110. https://doi.org/10.1021/cr068445e.
34. Jadhav, S.A.; Bongiovanni, R. Synthesis and Organic Functionalization Approaches for Magnetite (Fe3O4) Nanoparticles. *Adv. Mater. Lett.* **2012**, *3(5)*, 356- 361. https://doi.org/10.5185/amlett.2012.7381.
35. Amrousse R., Tsutsumi A., Bachar A., Lahcene D. N2O catalytic decomposition over nano-sized particles of Co-substituted Fe3O4 substrates. *Appl Catal A-Gen*. **2013**, *450*, 253–260. https://doi.org/10.1016/j.apcata.2012.10.036.
36. Sassykova, L.R.; Sassykova, A.R.; Kubekova, Sh. N.; Batyrbayeva, A.A.; Azhigulova, R. N.; Zhaxibayeva, Zh. M.; Kozhaisakova, M. A.; Zhusupova, L. A.; Sendilvelan, S.; Ponomarenko, O.I. Hydrogenation of aromatic nitro compounds to amines on nickel and iron-containing catalysts. *Rasayan J. Chem.* **2021**, *14(2)*, 1223-1229. https://doi.org/10.31788/ RJC.2021.1426124.
37. Liu, Z.; Miao, F.; Hua, W.; Zhao, F. Fe3O4 nanoparticles: Microwave-assisted Synthesis and Mechanism. *Mater. Lett.* **2012**, *67(1)*, 358-361. https://doi.org/10.1016/j.matlet.2011.09.095
38. Subash, M.; Chandrasekar, M.; Panimalar, S.; Inmozhi, C.; Uthrakumar, R. Synthesis, characterizations of pure and Co2+ doped iron oxide nanoparticles for magnetic applications. *Mater. Today: Proc.* **2022**, *56(6)*, 3413-3417. https://doi.org/10.1016/j.matpr.2021.10.340
39. Tulepov, M.; Mansurov, Z.; Sassykova, L.; Baiseitov, D.; Dalelhanuly, O.; Ualiev, Zh.; Gabdrashova, S.; Kudyarova, Z. Research of iron-containing concentrates of Balkhash deposit (Kazakhstan) for processing of low-grade coal. *J. Chem. Technol. Metall.* **2019**, *54(3)*, 531-538.
40. Jagadeesh, R. V.; Surkus, A.-E.; Junge, H.; Pohl, M.-M.; Radnik, J.; Rabeah, J.; Huan, H.; Schünemann, V.; Brückner, A.; Beller, M. Nanoscale Fe2O3-based catalysts for selective hydrogenation of nitroarenes to anilines. *Science* **2013**, *342*, 1073−1076.
41. Wei, H.; Liu, X.; Wang, A.; Zhang, L.; Qiao, B.; Yang, X.; Huang, Y.; Miao, S.; Liu, J.; Zhang, T. FeO x-supported platinum single-atom and pseudo-single-atom catalysts for chemoselective hydrogenation of functionalized nitroarenes. *Nat. Commun*. **2014**, *5*, 5634.
42. Macpherson, H. A.; Stoldt, C. R. Iron pyrite nanocubes: size and shape considerations for photovoltaic application. ACS Nano **2012**, 6, 8940−8949.
43. Steinhagen, C.; Harvey, T. B.; Stolle, C. J.; Harris, J.; Korgel, B. A. Pyrite nanocrystal solar cells: promising, or fool's gold? *J. Phys.Chem. Lett.* **2012**, *3*, 2352−2356.
44. Douglas, A.; Carter, R.; Oakes, L.; Share, K.; Cohn, A. P.; Pint, C. L. Ultrafine iron pyrite (FeS2) nanocrystals improve sodium−sulfur and lithium−sulfur conversion reactions for efficient batteries. *ACS Nano* **2015**, *9*, 11156−11165.

45. Li, L.; Cabán-Acevedo, M.; Girard, S. N.; Jin, S. High-purity iron pyrite (FeS2) nanowires as high-capacity nanostructured cathodes for lithium-ion batteries. *Nanoscale* **2014**, *6*, 2112−2118.
46. Li, Z.; Xiao, M.; Zhou, Y.; Zhang, D.; Wang, H.; Liu, X.; Wang, D.; Wang, W. Pyrite FeS2/C nanoparticles as an efficient bifunctional catalyst for overall water splitting. *Dalton Trans.* **2018**, *47*, 14917−14923.
47. Gao, M.-R.; Zheng, Y.-R.; Jiang, J.; Yu, S.-H. Pyrite-type Nanomaterials for Advanced Electrocatalysis. *Acc. Chem. Res.* **2017**, *50*, 2194−2204.
48. Mohapatra, J.; Mitra, A.; Tyagi, H.; Bahadur, D.; Aslam, M. Iron oxide nanorods as high-performance magnetic resonance imaging contrast agents. *Nanoscale* **2015**, *7*, 9174−9184.
49. Lucas, J. M.; Tuan, C.-C.; Lounis, S. D.; Britt, D. K.; Qiao, R.; Yang, W.; Lanzara, A.; Alivisatos, A. P. Ligand-Controlled Colloidal Synthesis and Electronic Structure Characterization of Cubic Iron Pyrite (FeS2) *Nanocrystals. Chem. Mater.* **2013**, *25*, 1615−1620.
50. Wadia, C.; Wu, Y.; Gul, S.; Volkman, S. K.; Guo, J.; Alivisatos, A. P. Surfactant-Assisted Hydrothermal Synthesis of Single phase Pyrite FeS2 Nanocrystals. *Chem. Mater.* **2009**, *21*, 2568−2570.
51. Jamei, M. R.; Khosravi, M. R., Anvaripour, B. Investigation of ultrasonic effect on synthesis of nano zero valent iron particles and comparison with conventional method. *Asia-Pac. J. Chem. Eng.* **2013**, *8*, 767-774.
52. Trinh, T. K.; Pham, V. T. H.; Truong, N. T. N.; Kim, C. D.; Park, C. Iron pyrite: Phase and shape control by facile hot injection method. J. Cryst. Growth 2017, 461, 53−59.
53. Thomson, J. W.; Nagashima, K.; Macdonald, P. M.; Ozin, G. A. From sulfur− amine solutions to metal sulfide nanocrystals: peering into the oleylamine− sulfur black box. *J. Am. Chem. Soc.* **2011**, *133*, 5036−5041.
54. Raabe, T.; Mehne, M.; Rasser, H.; Krause, H.; Kureti, S. Study on iron-based adsorbents for alternating removal of H2S and O2 from natural gas and biogas. *Chem. Eng. J.* **2019**, *371*, 738−749
55. Li, B.; Huang, L.; Zhong, M.; Wei, Z.; Li, J. Electrical and magnetic properties of FeS2 and CuFeS2 nanoplates. *RSC Adv.* **2015**, *5*, 91103−91107.
56. von Oertzen, G. U.; Skinner, W. M.; Nesbitt, H. W. Ab initio and XPS studies of pyrite (100) surface states. *Radiat. Phys. Chem.* **2006**, *75*, 1855−1860.
57. Jiang, F.; Peckler, L. T.; Muscat, A. J. Phase pure pyrite FeS2 nanocubes synthesized using oleylamine as ligand, solvent, and reductant. *Cryst. Growth Des.* **2015**, *15*, 3565−3572.
58. Dosumov, K.; Ergazieva, G.E.; Churina, D.Kh.; Tel'Baeva, M.M. Cerium-containing catalysts for converting ethanol into ethylene. *Russ. J. Phys. Chem.A* **2014**. *88(10)*, 1806–1808.
https://doi.org/10.1134/S0036024414100094.
59. Carriazo, J.; Guélou, E.; Barrault, J.; Tatibouët, J.M.; Molina, R.; Moreno, S. Synthesis of pillared clays containing Al, Al-Fe or Al-Ce-Fe from a bentonite: Characterization and catalytic activity. *Catal. Today* **2005**, *107-108*, 126-132. https://doi.org/10.1016/j.cattod.2005.07.157
60. Yergaziyeva, G.Y.; Dossumov, K.; Mambetova, M.M.; Kurokawa, H.; Baizhomartov, B. Effect of Ni, La, and Ce Oxides on a Cu/Al2O3 Catalyst with Low Copper Loading for Ethanol Non-oxidative Dehydrogenation. *Chem Eng Technol* **2021**, *44(10)*, 1890–1899. https://doi.org/10.1002/ceat.202100112
61. Shomanova, Z.; Safarov, R.; Tashmukhambetova, Z.; Sassykova, L.; Nosenko, Y.; Mukanova, R. Complex Research of Ferroalloys Production Wastes by Physical and Chemical Methods. *J. Chem. Technol. Metall.* **2021**, *56(3)*, 629-636.
62. Dehmani, Y.; Lgaz, H.; Alrashdi, A.A.; Lamhasni, T.; Abouarnadasse, S. Chung, Ill-M. Phenol adsorption mechanism on the zinc oxide surface: Experimental, cluster DFT calculations, and molecular dynamics simulations. *J. Mol. Liq.* **2021**, *324(15)*, 114993. https://doi.org/10.1016/j.molliq.2020.114993